JOURNAL OF AIRCRAFT
Vol. 32, No. 6, November–December 1995

Accuracy of a Propeller Model in Inviscid Flow

Per Lötstedt*
Saab Military Aircraft, S-58188 Linköping, Sweden

A model for computation of the time-averaged inviscid flow around airplane configurations with propellers is described. The propeller is replaced by an actuator disk in the Euler equations. The propeller forces are determined by a combined momentum-blade element theory. The computed results are compared to one-dimensional theory, calculations with a panel method, and wind-tunnel experiments. The tested configurations include a full aircraft at subsonic speed. The influence of the grid resolution and numerical parameters is also investigated.

Introduction

THE analysis of the flow generated by a propeller is important in the design phase of a propeller-driven aircraft. In the slipstream behind the propeller the flow properties are significantly different from the properties in the freestream. Surfaces of the configuration inside the slipstream experience other forces with the propeller on than they do in freestream flow. Accurate and relatively fast prediction of these forces and moments can often be obtained by large-scale computations.

The numerical solution of the time-dependent Navier–Stokes equations governing the flow around an airplane with rotating propellers is complicated and very costly. Simplifications of the equations are necessary in practice. Here we discuss three simplifying steps leading to the stationary Euler equations and an actuator disk model for the propeller. The propeller model is introduced into a program for solution of the Euler and Navier–Stokes equations on a computational domain partitioned into a number of blocks with structured grids.[1] The equations are discretized following Jameson[2,3] and the propeller forces are approximated by a combined momentum-blade element theory.[4,5] The flow variables in compressible flow are discontinuous at the disk. These jumps can be computed by a one-dimensional model, which is compared to calculations with the Euler equations. The accuracy of a numerical solution depends on the density of the grid and the artificial viscosity in the discretization. The influence of these numerical parameters on a propeller solution is investigated experimentally. The Euler equation approach is compared with a panel method for propeller simulations developed in Ref. 6. Comparisons with wind-tunnel measurements are made with both methods. The Euler solution is computed around SAAB 2000 with propellers. The results are compared to experimental data. Special attention is paid to the deviation of the slipstream from a cylindrical shape at the trailing edge of the wing.

Other developments of a time-averaged propeller simulation capability in solvers of the Euler equations are described.[7–12] The effect of the propeller is modeled by body forces in Ref. 7, whereas the propeller is represented by a disk in the other papers. In Refs. 10 and 12 the propeller model is implemented in a multiblock code for solution of the Euler equations similar to ours.[1] The treatment of the actuator disk is somewhat different here. The first tests with our approach are reported in Ref. 13 and further computational validation is found in Ref. 14.

Received Sept. 20, 1994; revision received May 1, 1995; accepted for publication May 26, 1995.

*Specialist, Aerodynamics Department.

In the next section a mathematical background to the actuator disk approximation is given. Then the numerical method is described briefly and the numerical results for four configurations are presented and compared to wind-tunnel data. Finally, some conclusions are drawn.

Equations

The flow in the slipstream behind a propeller is time dependent and very complicated. In order to reduce the complexity of the computational task three simplifications are made here: 1) inviscid flow, 2) a thin propeller disk, and 3) time-averaged variables. These three steps will now be discussed in more detail.

Inviscid Flow

The flow in the slipstream is turbulent and time dependent. A major reduction in model complexity is achieved if we assume that the velocity and pressure in the slipstream are well approximated by the Euler equations. The Euler equations including external forces generated by the propeller are

$$\begin{aligned}
&\frac{\partial \rho}{\partial t} + \frac{\partial(\rho u)}{\partial x} + \frac{\partial(\rho v)}{\partial y} + \frac{\partial(\rho w)}{\partial z} = 0\\
&\frac{\partial(\rho u)}{\partial t} + \frac{\partial(\rho u^2)}{\partial x} + \frac{\partial(\rho uv)}{\partial y} + \frac{\partial(\rho uw)}{\partial z} + \frac{\partial p}{\partial x} = f_x\\
&\frac{\partial(\rho v)}{\partial t} + \frac{\partial(\rho vu)}{\partial x} + \frac{\partial(\rho v^2)}{\partial y} + \frac{\partial(\rho vw)}{\partial z} + \frac{\partial p}{\partial y} = f_y\\
&\frac{\partial(\rho w)}{\partial t} + \frac{\partial(\rho wu)}{\partial x} + \frac{\partial(\rho wv)}{\partial y} + \frac{\partial(\rho w^2)}{\partial z} + \frac{\partial p}{\partial z} = f_z\\
&\frac{\partial(\rho E)}{\partial t} + \frac{\partial(\rho Eu + up)}{\partial x} + \frac{\partial(\rho Ev + vp)}{\partial y}\\
&\quad + \frac{\partial(\rho Ew + wp)}{\partial z} = Q
\end{aligned} \tag{1}$$

where ρ is the density, u, v, and w are the Cartesian velocity components, E is the total energy, p is the pressure, and Q is defined by

$$Q = uf_x + vf_y + wf_z$$

With the gas constant γ, Eq. (1) are closed by

$$p = (\gamma - 1)\rho[E - 0.5(u^2 + v^2 + w^2)]$$

The force $f = (f_x, f_y, f_z)$ is different from zero only in a region close to the propeller blades.

Propeller Disk

The extension of the propeller in the direction of its axis is small. By approximating the propeller by a thin disk the solution procedure is further simplified. The body or volume force f in Eqs. (1) is replaced by a surface force on the disk. The solution will be discontinuous at the disk and the flow variables will satisfy certain jump conditions. The position of these discontinuities is known and there is no need to develop jump capturing methods as it is for shock solutions. Instead the disk can be treated as an internal surface, where certain algebraic conditions must be fulfilled.

The jump conditions at the disk can be derived in the following way. Assume that the propeller axis is parallel to the x axis. This assumption is not necessary, but makes the expressions less cluttered by geometrical detail. Introduce the definitions

$$\begin{aligned} \boldsymbol{U} &= (\rho, \rho u, \rho v, \rho w, \rho E)^T \\ \boldsymbol{F} &= (\boldsymbol{F}_x, \boldsymbol{F}_y, \boldsymbol{F}_z) \\ \boldsymbol{F}_x &= [\rho u, \rho u^2 + p, \rho uv, \rho uw, u(\rho E + p)]^T \\ \boldsymbol{F}_y &= [\rho v, \rho vu, \rho v^2 + p, \rho vw, v(\rho E + p)]^T \\ \boldsymbol{F}_z &= [\rho w, \rho wu, \rho wv, \rho w^2 + p, w(\rho E + p)]^T \\ \boldsymbol{G} &= (0, f_x, f_y, f_z, Q)^T \end{aligned} \tag{2}$$

Then the integral form of the Euler Eqs. (1) is

$$\frac{\partial}{\partial t}\int_V \boldsymbol{U}\,\mathrm{d}V + \int_{\partial V} \boldsymbol{F}(\boldsymbol{U})\cdot \mathrm{d}\boldsymbol{S} = \int_V \boldsymbol{G}\,\mathrm{d}V \tag{3}$$

for an arbitrary volume V and its surface ∂V. In particular, let V be a cylinder containing the propeller with thickness ε in the x direction and such that $f \neq 0$ only in V. Now let $\varepsilon \to 0$. Since $\boldsymbol{U}$ is bounded at the propeller the first term on the left-hand side (LHS) in Eq. (3) vanishes. As $\varepsilon \to 0$ the volume forces f must grow so that the right-hand side (RHS) of Eq. (3) remains nonzero. Let $\delta(x)$ be the Dirac function, x_p the x coordinate of the disk, and

$$\boldsymbol{G}(x, y, z, t) = \tilde{\boldsymbol{G}}(y, z, t)\delta(x - x_p)$$

Then, as $\varepsilon \to 0$ it follows from Eq. (3) that

$$\boldsymbol{F}_{x2} = \boldsymbol{F}_{x1} + \tilde{\boldsymbol{G}}$$

where the indices 1 or 2 denote the values at the upstream and downstream sides of the disk, respectively. The jump conditions at the disk are explicitly

$$\begin{aligned} (\rho u)_2 &= (\rho u)_1 \\ (\rho u^2)_2 + p_2 &= (\rho u^2)_1 + p_1 + f_x \\ (\rho uv)_2 &= (\rho uv)_1 + f_y \\ (\rho uw)_2 &= (\rho uw)_1 + f_z \\ [\rho u(E + p/\rho)]_2 &= [\rho u(E + p/\rho)]_1 + Q \end{aligned} \tag{4}$$

In Eqs. (4) the bars on the disk surface quantities f and Q have been dropped. In general, all of the flow variables are discontinuous at the disk.

For all flows we conclude from Eqs. (4) that $v_2 = v_1 + f_y/(\rho u)_1$ and $w_2 = w_1 + f_z/(\rho u)_1$. If the flow is incompressible and $\rho_2 = \rho_1$, then in addition $u_2 = u_1$, $p_2 = p_1 + f_x$. Note that the relations (4) are valid also for time-dependent problems.

The variable Q must be evaluated on the disk. Suppose that u can be split into two parts close to the disk

$$u_n(x, y, z, t) = u_C(x, y, z, t) + u_d(y, z, t)\tanh[n(x - x_p)]$$

where u_C is continuous and u_d is half the jump in u at the disk. Then $u_1 = u_C - u_d$ and $u_2 = u_C + u_d$, and for large n we have $u \approx u_n$. The x component of Q in the integral on the RHS in Eq. (3) is integrated in the x direction

$$\begin{aligned} Q_x(y, z, t) &= \lim_{n\to\infty} \int_{-\varepsilon/2}^{\varepsilon/2} u_n f_x\,\mathrm{d}x \\ &= \lim_{n\to\infty} \int_{-\varepsilon/2}^{\varepsilon/2} u_n \tilde{f}_x \delta(x - x_p)\,\mathrm{d}x = \lim_{n\to\infty} u_n(x_p, y, z, t)\tilde{f}_x \\ &= 0.5(u_1 + u_2)\tilde{f}_x \end{aligned} \tag{5}$$

After a similar derivation for the y and z components of Q we find that Q can be chosen as

$$Q = 0.5[(u_1 + u_2)f_x + (v_1 + v_2)f_y + (w_1 + w_2)f_z] \tag{6}$$

Time-Averaged Equations

Even if the time-dependent Euler equations can be solved with propeller forces f varying in time on the disk in Eqs. (4) with a stationary grid at a reasonable cost, we can simplify the computational problem further by calculating the time-averaged flow variables. Then the steady-state solution of Eqs. (1) is determined with the time average of f over a period τ in the disk conditions (4). Assume that the time for one revolution of the propeller is τ and that a flow variable ϕ depends on f in the following way:

$$\phi(x, y, z, t) = \phi_0(x, y, z) + (\Psi f)(x, y, z, t)$$

where Ψ is an operator depending on the geometry of the configuration, Mach number, etc., such that $\Psi f = 0$ when $f = 0$. With the disk model (4) and the previous assumption the only time-dependent data for the differential equations is f. If Ψf depends linearly on f, so that

$$\frac{1}{\tau}\int_0^\tau \Psi f\,\mathrm{d}t = \Psi\frac{1}{\tau}\int_0^\tau f\,\mathrm{d}t \tag{7}$$

then we have for the time-averaged flow variable ϕ that

$$\frac{1}{\tau}\int_0^\tau \phi\,\mathrm{d}t = \phi_0(x, y, z) + \Psi\frac{1}{\tau}\int_0^\tau f\,\mathrm{d}t \tag{8}$$

i.e., by solving the Euler equations with time-averaged forces we obtain a correct time-averaged value of ϕ as the steady-state solution.

The relation (7) may not be satisfied except for special cases, but the time-averaged simplification rests on the assumption that Eq. (8) is approximately valid at least for some ϕ, e.g., the pressure. Such a special case is incompressible flow in one dimension. Then the Euler equations are

$$\begin{aligned} u_x &= 0 \\ u_t + uu_x + p_x/\rho_0 &= 0 \end{aligned} \tag{9}$$

on an interval $\mathcal{I} = (0, x_{\max})$ with the jump condition

$$\begin{aligned} u_1 &= u_2 \\ \rho_0 u_1^2 + p_1 + f_x(t) &= \rho_0 u_2^2 + p_2 \end{aligned} \tag{10}$$

at $x_p \in \mathcal{I}$ and boundary conditions

$$u(0, t) = u_0, \qquad p(0, t) = p_0 \tag{11}$$

By Eqs. (10) we find that at the disk

$$p_1 + f_x(t) = p_2 \tag{12}$$

It follows from Eqs. (9–11) that u is constant $\mathcal{P}$. Hence, by Eqs. (9) $p_x = 0$ and from Eqs. (11) and (12) we conclude

$$\begin{aligned} p(x, t) &= p_0, & x < x_p \\ p(x, t) &= p_0 + f_x(t), & x > x_p \end{aligned} \tag{13}$$

Here we have that

$$\begin{aligned} \bar{p}(x) &= \frac{1}{\tau}\int_0^\tau p(x, t)\,\mathrm{d}t = p_0, & x < x_p \\ \bar{p}(x) &= \frac{1}{\tau}\int_0^\tau p(x, t)\,\mathrm{d}t = p_0 + \frac{1}{\tau}\int_0^\tau f_x(t)\,\mathrm{d}t, & x > x_p \end{aligned} \tag{14}$$

and the time-averaged pressure $\bar{p}$ is obtained by solving stationary Eqs. (9) with a time-averaged jump condition.

Propeller Conditions in One Dimension

In one space dimension expressions for the flow variables behind the propeller, given the conditions ahead of the disk, can be derived from the discontinuity relations (4). In one dimension they are

$$\begin{aligned} \rho_1 u_1 &= \rho_2 u_2 \\ \rho_1 u_1^2 + p_1 + f &= \rho_2 u_2^2 + p_2 \\ h_1 + 0.5u_1^2 + q &= h_2 + 0.5u_2^2 \end{aligned} \tag{15}$$

In Eqs. (15) the enthalpy h and heat addition q are defined by the temperature T and

$$\begin{aligned} h &= E + (p/\rho) - 0.5u^2 = c_p T \\ q &= 0.5(u_1 + u_2)f/(\rho_1 u_1) \end{aligned} \tag{16}$$

where c_p is the specific heat at constant pressure. From the definition of total temperature T_0 (see Ref. 15), q is

$$\begin{aligned} q &= (h_2 + 0.5u_2^2) - (h_1 + 0.5u_1^2) = (c_p T_2 + 0.5u_2^2) \\ &\quad - (c_p T_1 + 0.5u_1^2) = c_p(T_{0_2} - T_{0_1}) \end{aligned} \tag{17}$$

By Eqs. (15) the propeller force contributes to the discontinuities in p and u in the following way:

$$f = (p_2 - p_1) + \rho_1 u_1(u_2 - u_1) \tag{18}$$

Introduce the dimensionless constant χ

$$\chi = f / (\rho_1 u_1^2)$$

Then from Eqs. (15) we have

$$p_1 + (1 + \chi)\rho_1 u_1^2 = p_2 + \rho_2 u_2^2$$

and with the Mach number definition

$$p_1 + (1 + \chi)\gamma M_1^2 p_1 = p_2 + \gamma M_2^2 p_2$$

or

$$\frac{p_2}{p_1} = \frac{1 + \gamma(1 + \chi)M_1^2}{1 + \gamma M_2^2} \tag{19}$$

Following the steps taken on p. 78 in Ref. 15 we arrive at similar expressions for u_2/u_1 and T_{0_2}/T_{0_1}

$$\frac{u_2}{u_1} = \left(\frac{M_2}{M_1}\right)^2 \frac{1 + \gamma(1 + \chi)M_1^2}{1 + \gamma M_2^2} \tag{20}$$

$$\frac{T_{0_2}}{T_{0_1}} = \left(\frac{M_2}{M_1}\right)^2 \frac{1 + 0.5(\gamma - 1)M_2^2}{1 + 0.5(\gamma - 1)M_1^2}\left[\frac{1 + \gamma(1 + \chi)M_1^2}{1 + \gamma M_2^2}\right]^2 \tag{21}$$

Combine Eqs. (16) and (17) to obtain

$$\frac{T_{0_2}}{T_{0_1}} = 1 + \frac{\chi u_1^2}{2c_p T_{0_1}}\left(1 + \frac{u_2}{u_1}\right) \tag{22}$$

Insert u_2/u_1 from Eq. (20) into Eq. (22). Suppose that the data u_1, M_1, T_{0_1}, ρ_1, and f are known to the left of the propeller disk. Then we have two different expressions for T_{0_2}/T_{0_1} in Eqs. (21) and (22) with M_2 as the unknown variable. This equation is easily solved numerically by, e.g., Newton iteration. Given M_1 and M_2 we have formulas for p_2/p_1 in Eq. (19), u_2/u_1 in Eq. (20), and a similar result for ρ_2/ρ_1 from the continuity of momentum in Eqs. (15). Hence, the flow variables are completely determined at the disk. The one-dimensional theory here is compared to three-dimensional steady computations shown next. A different derivation of similar results is found in Ref. 16, where f must be split into the two parts in Eq. (18) a priori.

For almost incompressible flow, when u_1 and u_2 and, therefore, M_1 and M_2 are small, we have from Eq. (19) that

$$p_2/p_1 \approx 1 + (f/p_1)$$

Then it follows from Eqs. (15) that

$$u_1 \approx u_2, \qquad \rho_1 \approx \rho_2$$

and from Eqs. (21), (20), and (19) that

$$T_{0_2}/T_{0_1} \approx p_2/p_1$$

Numerical Implementation

The Euler Eqs. (1) and (3) are approximated numerically by the cell-centered finite volume scheme in Refs. 3 and 2, respectively. Oscillations in the solution are avoided by adding a blend of second- and fourth-order artificial viscosity. On a Cartesian grid with constant step-size the approximation is of second-order accuracy. For the simple equation

$$\frac{\partial u}{\partial t} + \frac{\partial u}{\partial x} = 0$$

the fourth-order artificial viscosity is of the form

$$\frac{\theta h^3}{64}\frac{\partial^4 u}{\partial x^4} \tag{23}$$

where θ is a constant close to 1 and h is the step-size. The steady-state solution is computed by integrating the time-dependent equations forward in time by a three-stage explicit Runge–Kutta method until the residual of the equations is sufficiently small. The coefficients in the Runge–Kutta method are chosen for the best convergence rate. Suppose that $\boldsymbol{U}$ is the vector of length N with five unknown variables ρ, ρu, ρv, ρw, and ρE in each cell of the grid and $\boldsymbol{r}(\boldsymbol{U})$ is the system of N nonlinear equations to be solved after discretization in space. Let $\boldsymbol{U}^n$ be the nth iterate of the Runge–Kutta iteration. The iteration is interrupted after n steps if

$$\|\boldsymbol{r}(\boldsymbol{U}^n)\| = \left[N^{-1}\sum_{i=1}^{N} \boldsymbol{r}_i^2(\boldsymbol{U}^n)\right]^{1/2} \le \varepsilon \tag{24}$$

The parameter ε is taken to be sufficiently small. The criterion (24) is more reliable for propeller simulations than the usual one based on the continuity equation.

The propeller is represented by a disk between two layers of cells in the grid. The flow variables at the disk satisfy Eqs. (4). For the spatial discretization the variables are needed at cell boundaries, also at the disk. Since the values at the disk are not known, they are extrapolated from the upstream and downstream cells adjacent to the disk. In subsonic flow four characteristics enter the disk from the upstream side and one characteristic from the downstream side. Therefore, for stability the momentum in the x direction is taken from the downstream cell and the other four quantities in Eqs. (4) are taken from the upstream cells. Let u and d denote the values at the upstream and downstream side of the propeller. Then the equations for the upstream values are

$$\begin{aligned}(\rho u)_1 &= (\rho u)_d\\ (\rho u^2)_1 + p_1 &= (\rho u^2)_u + p_u\\ (\rho uv)_1 &= (\rho uv)_u\\ (\rho uw)_1 &= (\rho uw)_u\\ [\rho u(E + p/\rho)]_1 &= [\rho u(E + p/\rho)]_u\end{aligned} \tag{25}$$

and for the downstream values

$$\begin{aligned}(\rho u)_2 &= (\rho u)_d\\ (\rho u^2)_2 + p_2 &= (\rho u^2)_u + p_u + f_x\\ (\rho uv)_2 &= (\rho uv)_u + f_y\\ (\rho uw)_2 &= (\rho uw)_u + f_z\\ [\rho u(E + p/\rho)]_2 &= [\rho u(E + p/\rho)]_u + Q\end{aligned} \tag{26}$$

If $\boldsymbol{G}$ in Eqs. (2) is added on both sides of Eqs. (25), then we find that Eqs. (4) is fulfilled. With given RHSs, the variables upstream of the disk can be solved for in Eqs. (25) and the downstream values are given by Eqs. (26). There is an explicit solution to each of these systems of nonlinear equations. The fluxes over the cell boundaries at the disk for the finite volume scheme can now be computed. The disk values are determined in a similar fashion in Ref. 9.

The numerical boundary conditions in the far field are given by the Riemann invariants, except for the boundary where the propeller slipstream leaves the computational domain. There ρ, ρu, ρv, and ρw are extrapolated from the interior and p is specified to be the freestream pressure p_∞.

The propeller forces per area f_x, f_y, and f_y are computed by a combined momentum-blade element theory.[4,5] Input to the propeller model consists of geometry data for the propeller, the pitch angle β of the propeller blade, and the advance ratio J defined by

$$J = V_\infty/(N_p D)$$

where V_∞ is the freestream speed, N_p is the rotational speed of the propeller, and D is the diameter. Should β be unknown, an alternative input is the thrust coefficient C_F

$$C_F = T_p/(0.5\rho_\infty V_\infty^2 S)$$

where T_p is the propeller thrust, ρ_∞ is the freestream density, and S is a reference area. The lift of a two-dimensional section of a blade is computed from the local flow conditions with a Prandtl compressibility correction based on the Mach number. The components f_x, f_y, and f_z are then given by the lift force and the local geometry of the blade. The forces always vary in the radial direction on the disk. If the flow in front of the propeller is not parallel to the propeller axis, then they vary also in the azimuthal direction. In the present model, three-dimensional effects on the blade are not included. A refined model can be introduced easily as long as it only needs local flow variable data upstream and downstream of the propeller.

Computational Results

In this section we report on the computational results with four configurations of increasing geometrical complexity. The calculated values of the pressure coefficient c_p and the velocities are compared to theory, other computations, and to wind-tunnel measurements.

The accuracy of the propeller model depends on 1) the simplifications of the governing equations leading to the steady-state version of the Euler equations with a propeller disk; 2) the discretization errors due to the grid, the artificial viscosity, and the termination criterion in the iterative solution of the discretized equations; and 3) the approximation of the time-averaged propeller forces with the blade element theory.

The influence of the first source of error is best estimated by comparison with experimental data recorded by averaging over a sufficiently long time. The size of the numerical errors is found in computational experiments by changing the spatial resolution of the grid, the coefficients controlling the amount of viscosity in the discretization, and the interruption level in the iterations. These two causes of error in the computations are investigated here.

In Ref. 17 the third issue is discussed. Computation of the propeller forces by blade element theory is compared to a more elaborate approximation. There the flow around the propeller blades is determined by a panel method. That solution then defines the input to the actuator disk model in the Euler equations. The difference between these two approaches is small in the computational experiments in Ref. 17.

The four geometries in the comparisons are 1) a spinner on a sting, 2) an axisymmetric nacelle, 3) an axisymmetric nacelle and a wing, and 4) the civil aircraft SAAB 2000. The freestream speed is subsonic in all four cases.

Spinner on a Sting

The configuration is a spinner and a sting with a copy of the SAAB 340 propeller with four blades. This simple geometry was created to illustrate the discontinuities in the flow variables at higher Mach numbers and to compare with the one-dimensional theory developed earlier. In Fig. 1 the surface grid and the propeller disk are shown. The grid has about 25,000 cells. The angle of attack α is 0 deg, the freestream Mach number M_∞ is 0.6, the thrust coefficient C_F is 0.03, and the advance ratio J is 2. There are no wind-tunnel data available for this case.

The computed pressure p, density ρ, and axial momentum ρu along radii starting at the propeller axis are displayed in

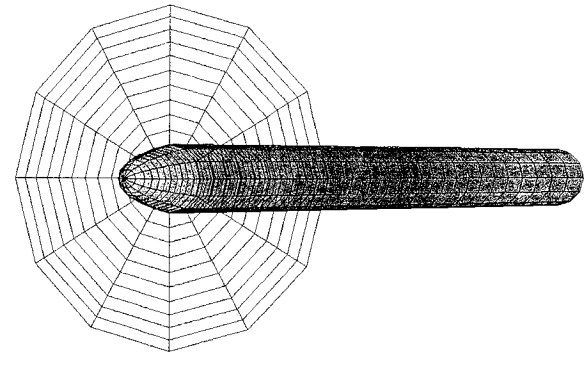

Fig. 1 Surface grid and propeller disk of the spinner on the sting.

Figs. 2–4, respectively. On the ordinate we have the distance from the axis scaled by the propeller radius r_p. Along the abscissas the variations of p, ρ, and ρu are plotted. The variables are compared at the inflow boundary (□), upstream of the disk (○), downstream of the disk (×), and in the middle of the sting (△). Equations (21) and (22) are solved for M_2 given the same data upstream of the disk as in the Euler calculations. Then p_2, ρ_2, and $(\rho u)_2$ on the downstream side of the disk are given by Eqs. (19), (20), and (15). These results downstream of the disk are marked by ▽.

Both p and ρ have lower values immediately in front of the disk compared to the values behind the disk. Far downstream p is almost constant and equal to the freestream pressure $p_\infty = 1/\gamma$ at the inflow boundary. The agreement downstream of the disk between the one-dimensional theory and the Euler solution is good. The three-dimensional effects seem to be negligible in this case.

Axisymmetric Nacelle

The flow around an axisymmetric nacelle with a propeller mounted on a sting is computed for investigation of the sensitivity of the solution to numerical parameters. The geometry is the same as in Ref. 18 for comparison with wind-tunnel results. The propeller is the same as discussed previously (and

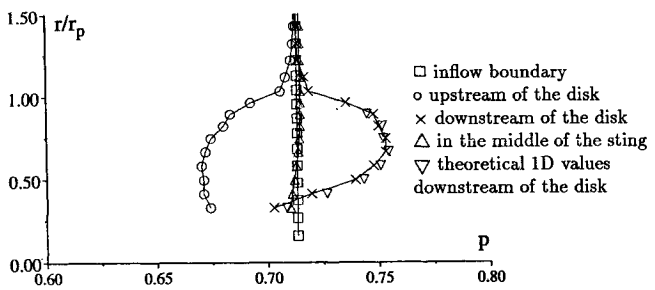

Fig. 2 Variation of p in the radial direction.

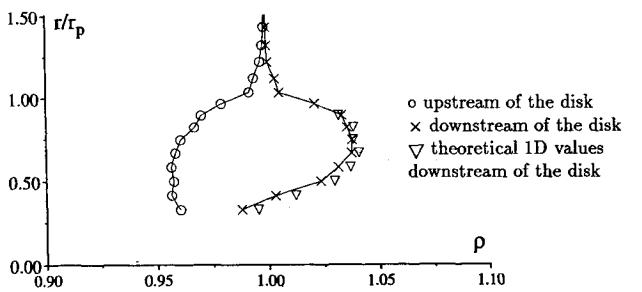

Fig. 3 Variation of ρ in the radial direction.

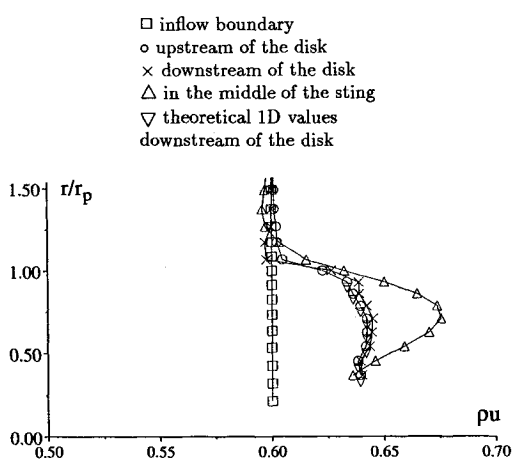

Fig. 4 Variation of ρu in the radial direction.

Table 1 Number of cells in different nacelle grids

Grid	x	r	φ	Symbol
1	68	24	12	▽
2	120	24	12	+
3	68	48	12	*
4	68	24	24	△
5	117	48	24	×

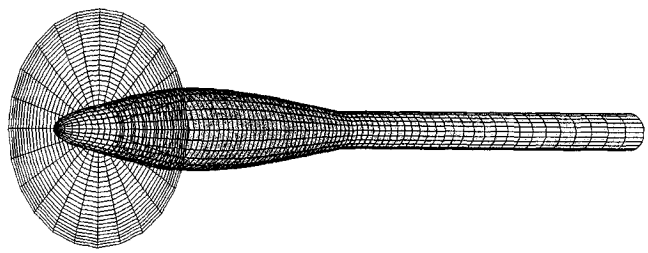

Fig. 5 Dense surface grid and propeller disk of the axisymmetric nacelle.

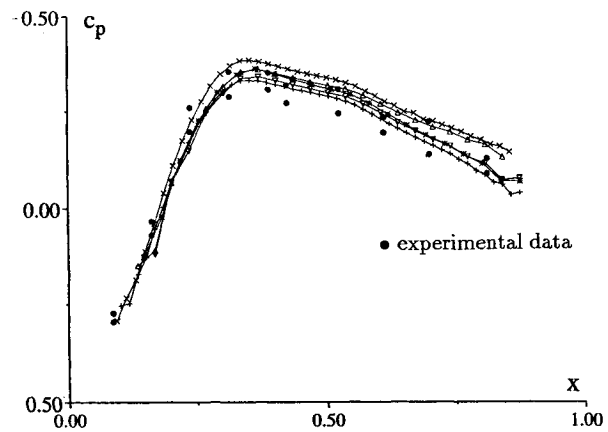

Fig. 6 Comparison of c_p values on the nacelle for the five grids in Table 1.

in Ref. 18). The configuration is shown in Fig. 5 with a dense surface grid and the propeller disk. In this case $\alpha = 0$ deg, $M_\infty = 0.15$, $C_F = 0.22$, and $J = 0.72$.

The polar coordinate system is chosen so that the x axis coincides with the propeller axis, the r axis is perpendicular to the propeller axis, and φ is the azimuthal angle. With $\alpha = 0$ deg the solution is axisymmetric. Five different grids are tested and the solutions are compared to wind-tunnel results. The number of cells in the different directions is listed in Table 1. If n_r is the number of cells in the r direction, then $n_r/2 - 2$ is the number of cells on the propeller.

There is a baseline coarse grid 1, this is refined in the three coordinate directions 2, 3, and 4 and the dense grid 5 is refined in all directions. The viscosity coefficient θ in Eq. (23) is 0.5. The length scale is such that the length of the nacelle is about 1 and all flow variables are also scaled to be about 1. The interruption parameter ε in Eq. (24) is 10^{-3}.

The values of the pressure coefficient c_p on the nacelle for the five grids are compared with experimental data in Fig. 6. The origin of the abscissa in the figure is at the propeller plane and the end of the nacelle is at $x = 0.95$. The measurements are marked by • and the symbols for the grids are found in Table 1. Since the wind-tunnel data are not completely axisymmetric, both the minimum and maximum value are plotted for each x station. From this variation of c_p we can estimate the error in the experimental data to be about $\Delta c_p = \pm 0.03$. In the figure the results from most of the grids are between the extremal experimental data. By varying the grid

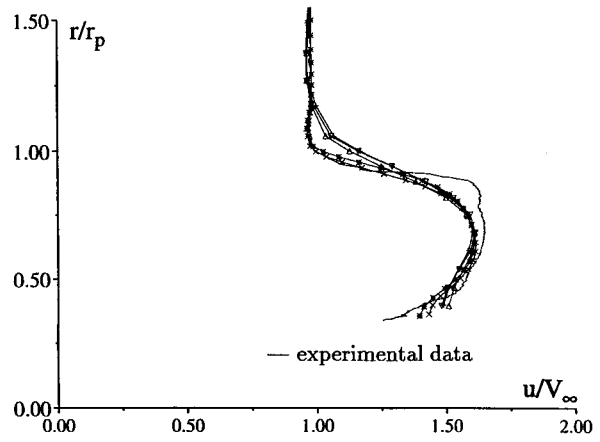

Fig. 7 Comparison of the variation of u for the five grids in Table 1.

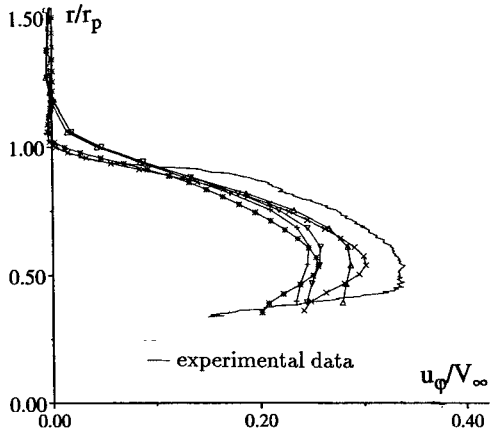

Fig. 8 Comparison of the variation of the circumferential velocity u_φ for the five grids in Table 1.

size as in Table 1, c_p deviates by at most $\Delta c_p = 0.05$ from the fine grid solution.

The computed velocity components in the x and φ directions are plotted in Figs. 7 and 8, respectively. The velocities are compared to experiments along a radius from the propeller axis at a station in the middle of the nacelle. The r coordinate scaled by the propeller radius r_p is on the ordinate and the velocity component scaled by V_∞ is on the abscissa. The wind-tunnel results are plotted with a solid line and the calculated data are marked by the symbols in Table 1.

We find in Fig. 7 that none of the grids are able to capture the behavior of u at the outer boundary of the slipstream. This discrepancy is probably due to the simplified model for computing the propeller forces, which is less accurate in the tip region of the blade. The best resolution of the slipstream in the neighborhood of $r = 1$ is, as expected, obtained with the grids 3 and 5 with high density in the r direction.

In Fig. 8 the circumferential speed u_φ is underestimated in the computations on all grids compared to the measurements. The highest speed is achieved with grids 4 and 5 with good resolution in the azimuthal direction. The absolute differences between the computed and measured peak speeds is about the same in Figs. 7 and 8. In the inner parts of the slipstream the difference between the solution on the finest grid and the coarsest grid is about 0.05 in both u/V_∞ and u_φ/V_∞.

The small velocity component in the radial direction is well represented on all grids when comparing to wind-tunnel measurements.

Different viscosity coefficients θ are compared in Fig. 9 on the coarse grid 1 for the circumferential velocity component. The peak speed is higher when $\theta = 0.5$ (+ in the figure) than

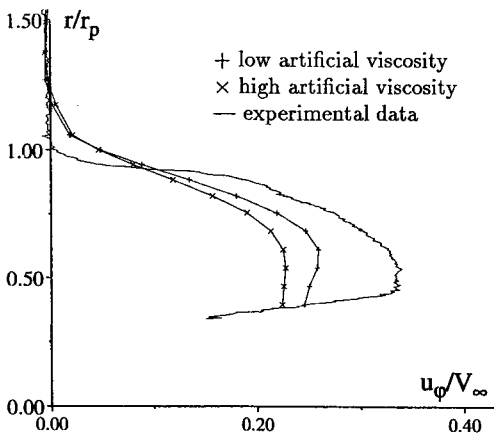

Fig. 9 Variation of the circumferential velocity u_φ for different artificial viscosities.

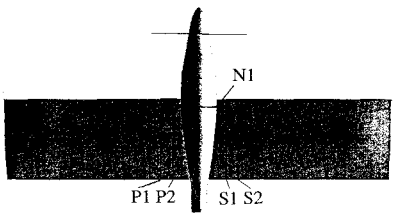

Fig. 10 Top view of the axisymmetric nacelle with a wing.

it is when $\theta = 1$ (×). The relative difference is much smaller in the x component and the c_p results over the nacelle.

The difference between solutions computed with different termination levels, $\varepsilon = 10^{-3}$ and 10^{-6} in Eq. (24), is barely visible in the plots.

The conclusion from these numerical experiments is that a good resolution of the grid in the radial direction is important for an accurate prediction of the velocity at the outer boundary of the slipstream. Also, the circumferential component is improved by more cells in the azimuthal direction.

Axisymmetric Nacelle with Wing

This configuration is a combination of the nacelle in the previous section and a wing with constant chord and a symmetric wing profile NACA $63_{(10)}A$—012. The propeller geometry here is also the same as on SAAB 340. The wing plane is a symmetry plane of the geometry. A top view of the nacelle, the wing, and the sting is found in Fig. 10. The flow and propeller parameters are $\alpha = 0$ and 5 deg, $M_\infty = 0.15$, $C_F = 0.22$, and $J = 0.72$. The propeller rotates in the clockwise direction looking downstream. The grid has 40 cells in the radial direction, 24 in the azimuthal direction, and a total of 96,000 cells. The number of cells on the propeller disk is 12 × 24. The viscosity parameter θ is 0.5.

The computed pressures and velocities with the Euler equations are compared to other computations with a panel program and the wind-tunnel results in Ref. 18. A higher-order panel program for subsonic speeds has been extended to handle also the vortical flow in the slipstream in Ref. 6. An approximate geometry of the slipstream and its inner structure is determined from the freestream flow over the nacelle. The amount of vorticity in the slipstream is given by the same forces per area f_x, f_y, and f_z as in Eqs. (4) and they are calculated by the same blade element approximation as in the Euler equations.

In the first case $\alpha = 0$ deg. Then the flow is antisymmetric in the sense that the solution on top of one wing is equal to the solution at the bottom of the other wing. The computed solutions with the Euler and panel methods have this property and the wind-tunnel measurements almost have it.

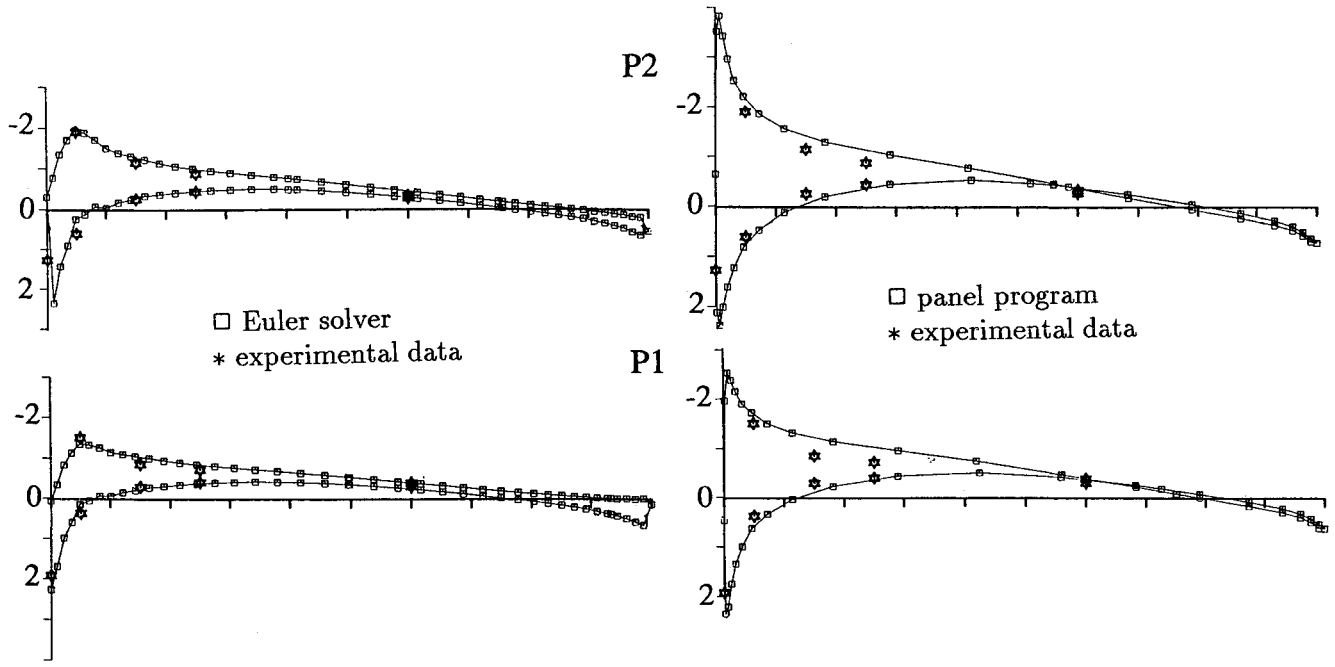

Fig. 11 Comparison of c_p values at $\alpha = 0$ deg at two wing sections P1 and P2 in Fig. 10.

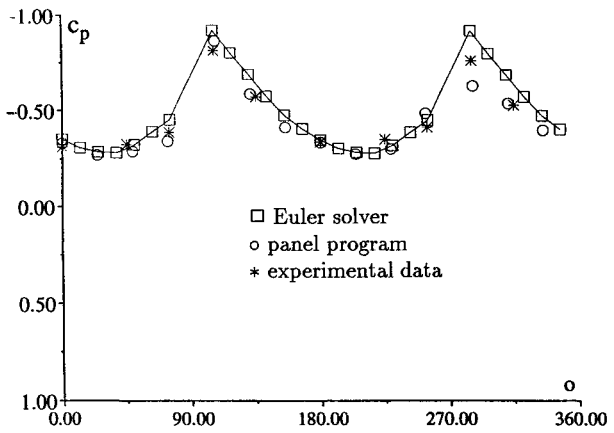

Fig. 12 Comparison of c_p values at $\alpha = 0$ deg at station N1 in Fig. 10.

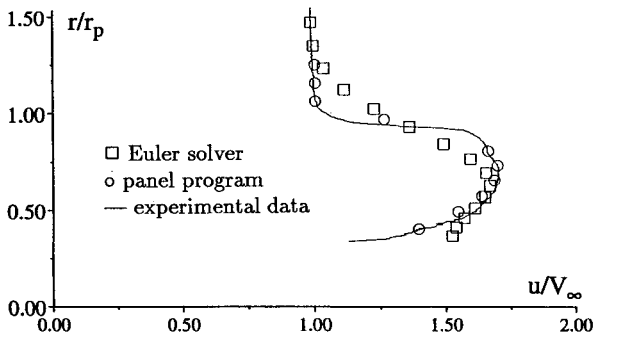

Fig. 13 Comparison of the variation of u at $\alpha = 0$ deg at station N1 in Fig. 10.

The c_p values at two wing sections P1 and P2, defined in Fig. 10, are compared in Fig. 11. To the left the Euler solution (□) and to the right the panel solution (□) are plotted with the wind-tunnel data (*). The Euler data are closer to the experiments. The difference between the solutions at the leading edge may be due to compressibility effects and a coarser surface grid in the Euler solution. Note the jump in c_p at the trailing edge in the results to the left. This is caused by a shearing of the slipstream to the port side above the wing and to the starboard side below the wing with our direction of rotation of the propeller. This phenomenon is observed both in wind-tunnel experiments[19,20] and in Euler computations[14] and is discussed later (cf. Fig. 17). The geometry of the slipstream in the panel method does not model this shift. In the Euler computations there is a sensitivity in c_p to the θ parameter in the artificial viscosity in Eq. (23) at the trailing edge of the wing. It should be chosen as small as possible without introducing spurious oscillations in the solution. The amount of artificial viscosity affects the flow pattern right behind the trailing edge, where a vortex sheet leaves the wing, and has an influence on the lift of the wing. A similar sensitivity is present in the formulation of the Kutta condition at the trailing edge in panel methods.

The error in c_p over the wings in the Euler solution due to the grid can be estimated in the following way. In this case the flow is almost incompressible. From Bernoulli's relation it follows that:

$$c_p = 1 - (V/V_\infty)^2, \qquad V = (u^2 + v^2 + w^2)^{1/2}$$

Thus,

$$\Delta c_p = -2V\Delta V/V_\infty^2$$

The difference in V/V_∞ between grid 4, which has approximately the same resolution of the propeller as the grid around the wing–nacelle configuration, and the finest grid 5 in Table 1, is about 0.02 in the slipstream in Figs. 7 and 8. Since $V/V_\infty \approx 1.6$ we conclude that Δc_p would change by at most 0.06 over the wing with a refined grid in the r and x directions. Because of the antisymmetry we can compare the measured data on the upper part of the port side wing with the lower part of the starboard wing and vice versa. These c_p values should be equal on the two wings. The data are not presented here, but in the deviation from antisymmetry the uncertainty is estimated to be $\Delta c_p = \pm 0.1$.

In Fig. 12 the wind-tunnel (*), Euler (□), and panel method (○) results for the pressure coefficient are compared at station N1 in Fig. 10 along the periphery of the nacelle. The abscissa here is the φ angle, which is 0 on top of the nacelle. The

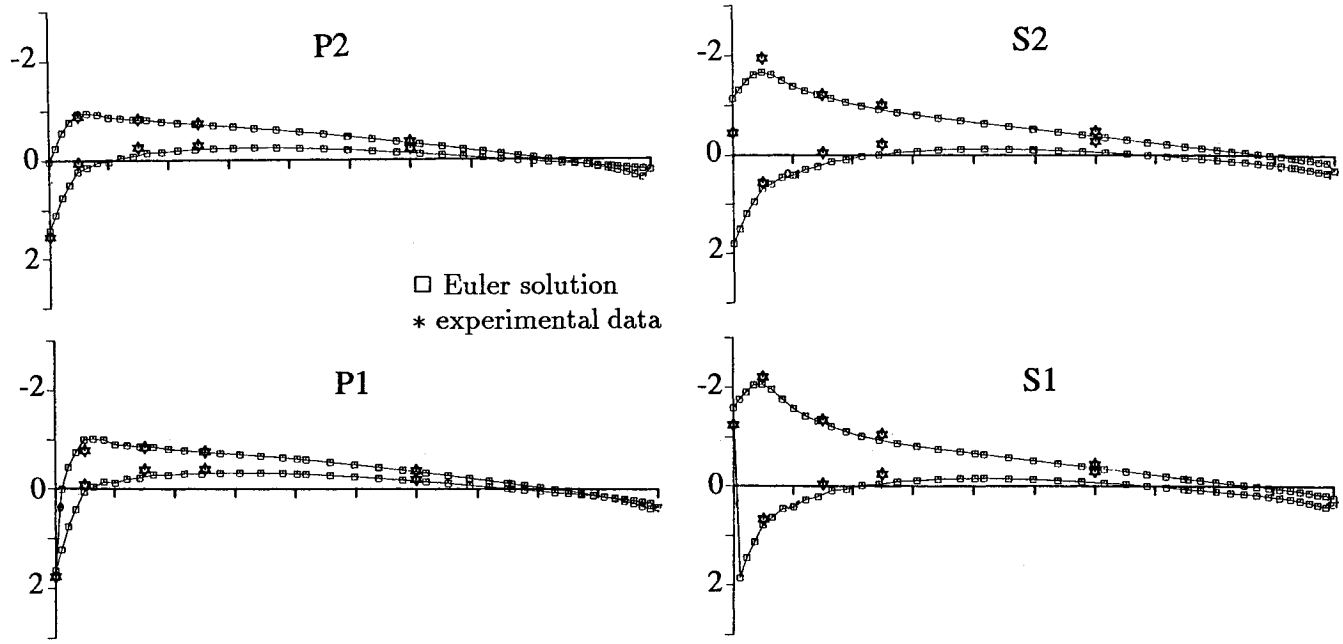

Fig. 14 Comparison of c_p values at $\alpha = 5$ deg at P1, P2, S1, and S2 in Fig. 10.

agreement between the calculations and the experiments is good. By Fig. 6 it follows that the calculated c_p on the nacelle is not so sensitive to the grid resolution.

The speed in the x direction is plotted in Fig. 13 at station N1 in the radial direction with $\varphi = 0$ obtained with the two computational methods and in the wind tunnel. The r coordinate on the ordinate is scaled by the propeller radius and the speed on the abscissa is scaled by the freestream speed V_∞. The experiments are displayed with a solid line. The panel method (○) is more accurate than the Euler method (□) here, because it models the outer boundary of the slipstream much better than the Euler grid, which obviously is too coarse (cf. Fig. 7). The reason for the better resolution of the panel method is that in Ref. 14 the vortical flow inside the slipstream is represented by discrete cylindrical surfaces with vorticity. A sharp outer boundary of the slipstream is given by the largest of these cylinders.

For propeller slipstream computations the advantages of the panel method is that only a surface grid of the configuration is needed and that the CPU time to obtain a solution is relatively short. For the SAAB 2000 model in the next example the CPU time on Cray Y-MP for the Euler code can be up to 50 times longer. A geometrical structure for the propeller wake is necessary in a panel method. The wake is fixed in Ref. 6, but can in principle be relaxed in the computations. No such predetermined slipstream geometry is used in the Euler equation solver. The agreement with wind-tunnel data is in general better for the Euler solution, in particular for higher M_∞, $\alpha \neq 0$ deg, and complex configurations. At the outer boundary of the slipstream the almost discontinuous behavior of the velocity is, however, better captured by the panel method. A particularly fine grid is needed here in the Euler calculations.

The c_p calculations with the Euler equations are in good agreement with the experiments for $\alpha = 5$ deg in Fig. (14). The difference is small between the computed and measured c_p values also on the nacelle (cf. Fig. 12).

Comparisons are made in Eq. 14 with the wind-tunnel experiments for a nonaxisymmetric nacelle with a wing in Ref. 18. The agreement between the calculated and measured data is as good as it is for the axisymmetric geometry here.

SAAB 2000

A grid has been generated around a half model of the propeller airplane SAAB 2000. The air inlet to the engine has been closed and the rear part of the nacelle is modified. The grid has more than 800,000 cells and is fairly dense in the vicinity of the wing, the nacelle, and the propeller disk. The number of cells on the propeller in the radial and azimuthal directions is 12 and 76, respectively. The grid around the port side of the airplane and its image in the symmetry plane is depicted in Fig. 15.

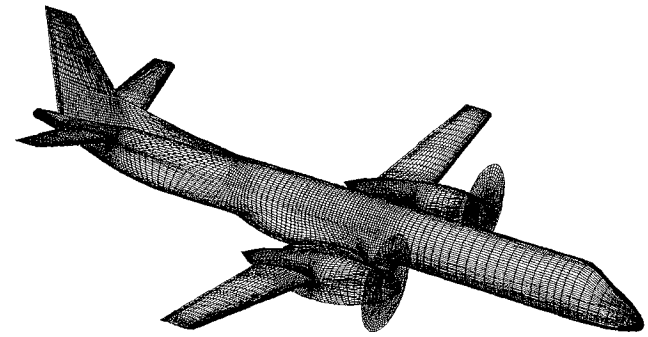

Fig. 15 Surface grid on SAAB 2000 with propeller disks.

A comparison between computed and measured c_p values on the port side wing is found in Fig. 16 at $M_\infty = 0.18$, $\alpha = 0.67$ deg, $J = 0.8$, and C_F about 0.13 corresponding to a takeoff case. Two of the wing sections are located inside the slipstream. Standing in front of the propeller it rotates in the counterclockwise direction. The error $\|r(U^0)\|$ in Eq. (24) in the initial solution U^0 has been reduced by three decades when the iteration to solve the nonlinear equations are terminated after n steps, i.e.,

$$\|r(U^n)\|/\|r(U^0)\| < 10^{-3}$$

The Euler solution is plotted with □ and the experiments with ∗, and the c_p scale is the same for all sections. The agreement between computational results and wind-tunnel data is quite good. A similar agreement is obtained in another comparison in Ref. 14 for a cruise case with $J = 3.0$ and $C_F \approx 0.015$. The discussion of the computational errors in the previous section is applicable also here.

In Fig. 17 the contours of the difference in total pressure $\Delta p_t = p_t - p_{t\infty}$ are shown in a plane right behind the trailing edge of the port side wing looking in the upstream direction.

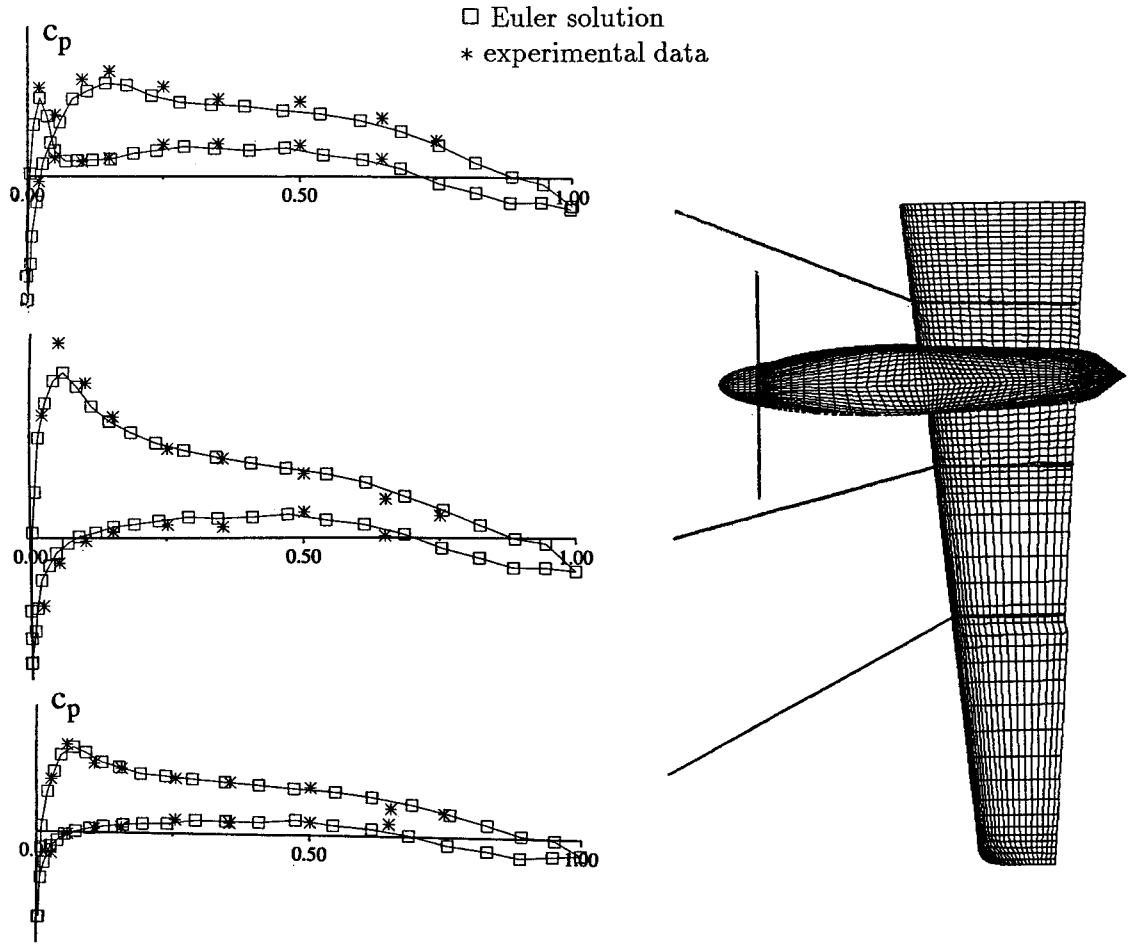

Fig. 16 Comparison of c_p values.

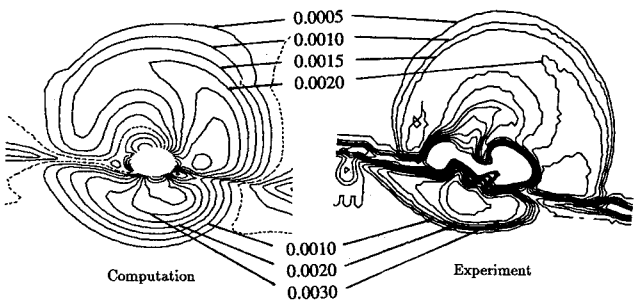

Fig. 17 Total pressure contours in a plane behind the trailing edge of the port side wing.

The computations (left) are compared with the experiments (right). The dashed line to the left is the isobar for $p_{t\infty}$. The slipstream rotates in the clockwise direction in the plots. Here, $M_\infty = 0.18$, $\alpha = 0$ deg, $J = 2.0$, and $C_F = 0.017$. The static pressure p_∞ is 1 and, therefore, $p_{t\infty}$ is 1.023. The distance between the isobars in the figure is 0.0005. The geometry of the nacelle behind the wing in the computational model is different from the geometry in the experiments. In the computations the nacelle is extended by a cone (see Fig. 16) to avoid the flat base in the wind-tunnel model. On the upper side of the wing the slipstream is shifted to the right and on the lower side to the left. Also in Refs. 19 and 20 this effect is verified experimentally. The same phenomenon is present in the wake behind a ship propeller and a rudder.[21] When comparing the calculations and the measurements we observe that the levels and patterns of p_t are almost equal in the slipstream above and below the wing. The geometry of the outer boundary of the slipstream differs below the wing. The shearing of the slipstream is more pronounced in the experiments. This may be due to the sensitivity of the slipstream behind the wing to the artificial viscosity parameter θ in Eq. (23), which is 1 in these computations.

Conclusions

A model for computation of propeller slipstream effects has been incorporated into a program for solution of the Euler equations around general aircraft configurations. For a high subsonic Mach number the calculated results have been compared to one-dimensional theory with good agreement. The sensitivity to the choice of numerical parameters has been investigated. The conclusion is that for accurate prediction of the velocities in the slipstream good grid resolution is needed, in particular at the outer edge of the slipstream. The c_p values are less sensitive. For the best accuracy at the trailing edge of a wing the parameter for the artificial viscosity should be chosen as small as possible. The solution of the Euler equations has been compared to the results from a panel method and wind-tunnel experiments. In spite of the fact that it is easier and faster to use a panel method for subsonic flow, the Euler solver is the preferred method because of its ability to capture the shape of the slipstream automatically. Furthermore, we expect it to be more accurate for higher Mach numbers. The solution has been computed around a full airplane configuration, SAAB 2000, and the results have been compared to measured data. The agreement is good for c_p values on the wing. The shearing of the slipstream behind the wing is observed in both the computed and measured total pressures.

Acknowledgment

Henrik Olofsson created the grid around SAAB 2000 and Lars Olsson provided the wind-tunnel data for that aircraft.

References

[1]Lötstedt, P., and Sillén, M., "Multigrid Multiblock Solver of the Stationary Euler and Navier-Stokes Equations," SAAB Military Aircraft, Rept. L-0-1 R148, Linköping, Sweden, Nov. 1993.

[2]Jameson, A., "Computational Transonics," *Communications in Pure and Applied Mathematics*, Vol. XLI, 1988, pp. 507–549.

[3]Jameson, A., Schmidt, W., and Turkel, E., "Numerical Solutions of the Euler Equations by Finite Volume Methods Using Runge-Kutta Time-Stepping Schemes," AIAA Paper 81-1259, Jan. 1981.

[4]Lock, C. N. H., Pankhurst, R. C., and Conn, J. F. C., "Strip Theory Method of Calculation for Airscrews on High-Speed Aeroplanes," ARC TR, R & M 2035, British Aeronautical Research Council, His Majesty's Stationery Office, London, Oct. 1945.

[5]McCormick, B. W., Jr., *Aerodynamics of V/STOL Flight*, Academic, New York, 1967.

[6]Lötstedt, P., "Propeller Slip-Stream Model in Subsonic Linearized Potential Flow," *Journal of Aircraft*, Vol. 29, No. 6, 1992, pp. 1098–1105.

[7]Whitfield, D. L., and Jameson, A., "Three-Dimensional Euler Equation Simulation of Propeller-Wing Interaction in Transonic Flow," AIAA Paper 83-0236, Jan. 1983.

[8]Yu, N. J., and Chen, H. C., "Flow Simulations for Nacelle-Propeller Configurations Using Euler Equations," AIAA Paper 84-2143, Aug. 1984.

[9]Samant, S. S., and Yu, N. J., "Flow Prediction for Propfan Engine Installation Effects on Transport Aircraft at Transonic Speeds," NASA CR 3954, 1986.

[10]Amendola, A., Tognaccini, R., Boerstoel, J. W., and Kassies, A., "Validation of a Multi-Block Euler Flow Solver with Propeller-Slipstream Flows, Validation of Computational Fluid Dynamics," Vol. 2, CP-437, AGARD, Neuilly-sur-Seine, France, 1988, pp. P1-1–P1-15.

[11]Kuijvenhoven, J. L., "Validation of Propeller Slipstream Calculations Using a Multi-Block Euler Code," AIAA Paper 90-3035, Aug. 1990.

[12]Nishida, B. A., Langhi, R. G., and Bencze, D. P., "A Multiblock/Multigrid Euler Analysis of a Propfan Transport with Wing-Mounted Nacelles Including Slipstream Effects," AIAA Paper 91-0706, Jan. 1991.

[13]Einarsson, A., "Improved Propeller Modelling Using the Combined Momentum-Blade Element Theory in an Euler Flow Solver," SAAB Military Aircraft, Rept. L-0-1 R144, Linköping, Sweden, 1992.

[14]Lötstedt, P., "Properties of a Propeller Model in the Stationary Euler Equations, Computational Fluid Dynamics 94," *Proceedings of the 2nd European Computational Fluid Dynamics Conference*, edited by S. Wagner, E. H. Hirschel, J. Périaux, and R. Piva, Wiley, New York, Sept. 1994, pp. 594–601.

[15]Anderson, J. D., Jr., *Modern Compressible Flow*, McGraw-Hill, New York, 1990.

[16]Delano, J. B., and Crigler, J. L., "Compressible Flow Solutions for the Actuator Disk," NACA RM L53A07, Washington, DC, March 1953.

[17]Schipholt, G. J., Voogt, N., and Van Hengst, J., "Investigation of Methods for Modeling Propeller-Induced Flow Fields," AIAA Paper 93-0874, Jan. 1993.

[18]Samuelsson, I., "Low Speed Wind Tunnel Investigation of Propeller Slipstream Aerodynamic Effects on Different Nacelle/Wing Combinations," Aeronautical Research Inst. of Sweden, Pt. 1, FFA TN 1987-22, Stockholm, Sweden, June 1987.

[19]Aljabri, A. S., and Hughes, A. C., "Wind Tunnel Investigation of Propeller Slip-Stream Interaction with Nacelle/Wing/Flap Combinations," AGARD Paper 21, Oct. 1984.

[20]Johnson, R. T., Witkowski, D. P., and Sullivan, J. P., "Experimental Results of a Propeller/Wing Interaction Study," Society of Automotive Engineers, SAE Paper 910998, April 1991.

[21]Li, D.-Q., "Investigation of Propeller-Rudder Interaction by Numerical Methods," Ph.D. Dissertation, Dept. of Naval Architecture and Ocean Engineering, Chalmers Univ. of Technology, Gothenburg, Sweden, March 1994.